

 Open access • Journal Article • DOI:10.1007/S10652-017-9512-5

## Ritter's dry-bed dam-break flows: positive and negative wave dynamics

— [Source link](#) 

Oscar Castro-Orgaz, Hubert Chanson





**Institutions:** University of Córdoba (Spain), University of Queensland

**Published on:** 09 Feb 2017 - Environmental Fluid Mechanics (Springer Netherlands)

**Topics:** Inviscid flow, Shallow water equations, Riemann problem, Fluid mechanics and Discontinuous Galerkin method

Related papers:

- [Dam-Break Flood in a Prismatic Dry Channel](#)
- [Riemann wave description of erosional dam-break flows](#)
- [Dam-break flows during initial stage using SWE and RANS approaches](#)
- [A Moving Boundary Wave Run-Up Model](#)
- [Quasi-exact solution of the Riemann problem for generalised dam-break over a mobile initially flat bed](#)

Share this paper:    

View more about this paper here: <https://typeset.io/papers/ritter-s-dry-bed-dam-break-flows-positive-and-negative-wave-2szjas7zk3>

## **Ritter's dry-bed dam-break flows: Positive and negative wave dynamics**

Oscar Castro-Orgaz<sup>1</sup> and Hubert Chanson<sup>2</sup>

### **Abstract**

Dam-break flood waves are associated with major environmental disasters provoked by the sudden release of water stored in reservoirs. Ritter found in 1892 an analytical solution to the wave structure of an ideal fluid released during an instantaneous dam failure, propagating over initially dry horizontal terrain. This solution, though ideal, hence frictionless, is widely used to test numerical solutions of the Shallow Water Equations (SWE), and as educational tool in courses of fluid mechanics, given that it is a peculiar case of the Riemann problem. However, the real wave structure observed experimentally differs in a major portion of the wave profile, including the positive and negative fronts. Given the importance of an accurate prediction of the dam break wave, the positive and negative wave portions originating from the breaking of a dam with initially dry land on the tailwater reach are revisited in this work. First, the propagation features of the dry-front are investigated using an analytical boundary-layer type model (Whitham/Dressler/Chanson model) constructed matching an (outer) inviscid dynamic wave to an (inner) viscous diffusive wave. The analytical solution is evaluated using an accurate numerical solution of the SWE produced using the MUSCL-Hancock finite-volume method, which is tested independently obtaining the solution based on the discontinuous Galerkin finite-element method. The propagation features of the negative wave are poorly reproduced by the SWE during the initial stages of dam break flows, and, thus, are then investigated using the Serre-Green-Naghdi equations for weakly-dispersive fully non-linear water waves, which are solved using a finite volume-finite difference scheme.

**Keywords:** Dam-break wave; Dry-front; Rarefaction wave; Ritter's solution; Saint-Venant equations; Serre-Green-Naghdi equations

<sup>1</sup>University of Cordoba, Spain, Campus Rabanales, Leonardo Da Vinci building, E-14071, Cordoba, Spain. E-Mail: [ag2caoro@uco.es](mailto:ag2caoro@uco.es) (author for correspondence)

<sup>2</sup>The University of Queensland, School of Civil Engineering, Brisbane QLD 4072, Australia. Email: [h.chanson@uq.edu.au](mailto:h.chanson@uq.edu.au).

## 1 Introduction

The sudden release of the water stored in a reservoir due to an instantaneous dam collapse can lead to serious environmental problems in the downstream valley, risk to human life, and severe economical damage. Thus, dam-break flows are a major concern in hydraulic and environmental engineering practice [1]. The hydraulic prediction of the wave resulting from the breaking of a dam gained impulse during the World War II, given the risk of dam destruction by military action [2]. In modern times, it is a major disaster linked to un-frequent engineering failure (Fig. 1a), but the hydraulic phenomenon is basically the same occurring in canals during the sudden gate operation [3, 4]. The dam break flood wave after the instantaneous failure of a dam propagates along natural waterways involving uneven beds, non-prismatic cross sections, and wet-dry fonts [5] (Fig. 1b). These problems are efficiently tackled using modern shock-capturing methods for the solution of the shallow-water flow equations. However, before attempting to solve real-life problems, where there is a need to deal with the peculiar constraints imposed by nature, it is an accepted practice to check numerical models using simple, idealized test cases. It cannot be expected to solve with any accuracy a complex real flow problem if a simplified and ideal test is not adequately addressed by a numerical model. In this context, Ritter's ideal dry-bed dam break solution for a rectangular and horizontal channel (see Appendix II) [6] is still today, after more than a century, a tool of wide use by modelers [5, 7]. It is also a very important material for teaching purposes in undergraduate courses of hydraulics and fluid mechanics [1, 3].

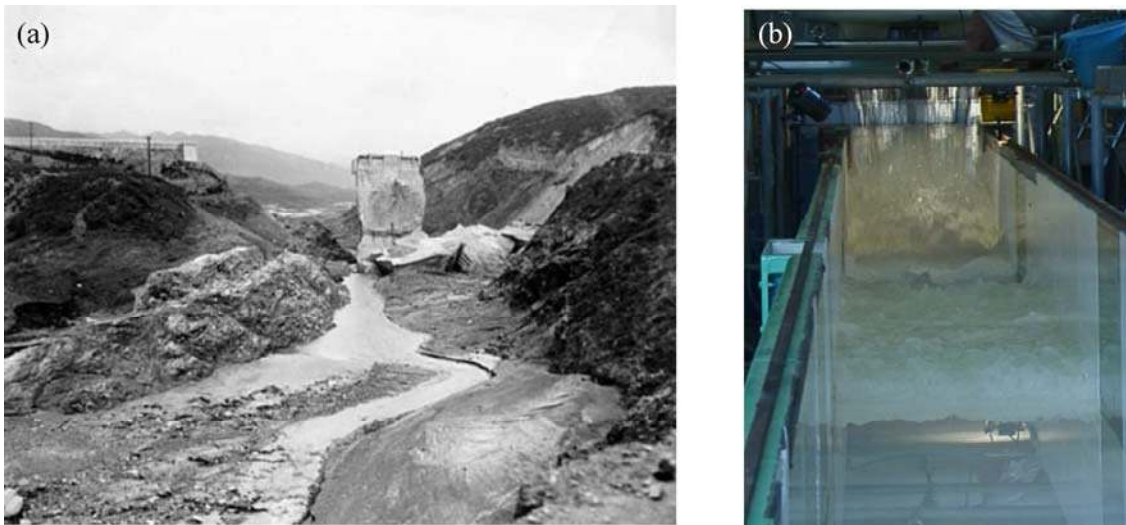


Figure 1 (a) Example of instantaneous dam break: the St Francis dam, USA (Courtesy of Santa Clarita Valley Historical Society) - Looking upstream at the dam wall ruins (b) experimental test of dam break wave, where the turbulence at the dry-bed front is visible

The shallow-water flow equations, or Saint-Venant equations are, for a frictionless and horizontal channel of prismatic and rectangular cross-section [1, 3, 8]

$$\frac{\partial h}{\partial t} + U \frac{\partial h}{\partial x} + h \frac{\partial U}{\partial x} = 0, \quad (1)$$

$$\frac{\partial U}{\partial t} + U \frac{\partial U}{\partial x} + g \frac{\partial h}{\partial x} = 0. \quad (2)$$

Here  $h$  is the water depth,  $U$  the depth-averaged velocity positive downstream in the  $x$ -direction,  $t$  is the time,  $x$  the horizontal coordinate with  $x = 0$  at the dam wall, and  $g$  the gravitational acceleration.

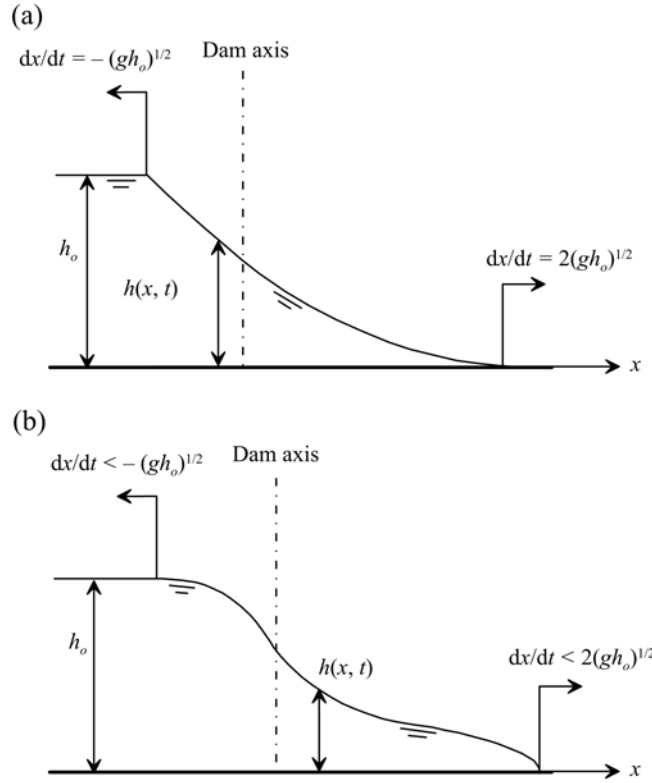


Figure 2 Instantaneous dam-break flow (a) Ritter's idealized wave (b) real wave structure observed experimentally [10]

Equations (1)-(2) are obtained from the Euler equations assuming that the vertical accelerations can be neglected, and that the velocity profile in the  $x$ -direction is uniform across the water layer of thickness  $h$  [1, 5]. Ritter's solution to Eqs.(1)-(2) for the instantaneous failure of a dam is (Fig. 2a)

$$h = \frac{1}{9g} \left[ 2(gh_o)^{1/2} - \frac{x}{t} \right]^2, \quad (3)$$

$$U = \frac{2}{3} \left[ \frac{x}{t} + (gh_o)^{1/2} \right], \quad (4)$$

with  $h_o$  as the water depth in the reservoir at the initiation of the dam collapse. The idealized solution given by Eqs. (3)-(4) is widely used to check numerical solutions of Eqs. (1)-(2). Further, in the context of fluid dynamics, it is a particular case of the Riemann problem, with the state-vector at one side of the discontinuity implying dry-bed conditions, and a motionless state at the other side of the interface [5, 9]. It is well-known based on a generalized solution of the Riemann problem that Ritter's solution is a particular rarefaction wave. The solution involves a similarity structure of the  $(h, U)$  predictors, depending solely on the coordinate  $(x/t)$ . The wave structure includes a positive dry-bed front propagating at speed  $2(gh_o)^{1/2}$ , and a negative front spreading back at rate  $-(gh_o)^{1/2}$  over the still water (Fig. 2a) (see Jain [3] or Toro [5] for detailed derivations). We denote as the positive wave the portion of the solution for any  $x > 0$  and  $t > 0$ , with the dam axis located at  $x = 0$ . Likewise, the negative wave is the solution at coordinate points  $x < 0$  for any time. The propagation speed of the positive and negative wave fronts is information of particular interest for natural hazard assessment and planning for an eventual evacuation of population from the tailwater reach of a river.

However, detailed experimental observations [10, 17] indicated a number of features not accounted for by Ritter's idealized wave structure. In particular, Ritter's prediction of the propagation speeds of the waves is not accurate. Near the front of the positive wave, the frictional resistance and

turbulence dominates the flow [11, 12, 13, 14] (see Fig. 1b), and cannot be ignored. As result of these real fluid flow features, the free surface profile in the “tip-portion” of the positive wave changes its curvature from the positive values indicated by the parabolic-law by Ritter [see Eq. (3)] to negative values [10, 14, 15] (See Fig. 2b). Consequently, the positive front propagates much slower than predicted by Ritter's theory [10]. Given the importance of flow resistance on the positive wave propagation, more advanced solutions were attempted in the literature to overcome the limitations of Ritter's theory. The effect of flow resistance on the dam break wave was considered analytically by Dressler [11], Whitham [12], and Chanson [14]. Chanson [14] expanded Whitham's [12] conceptual model which is based on the assumption that near the positive front the resistance forces are exactly balanced by pressure forces, and flow accelerations are therefore ignored. This simplified solution at the tip portion is then matched to the inviscid dynamic wave model, corresponding to Ritter's solution, away front the front. The result is a simplified analytical solution of Saint-Venant equations, much in the sense of boundary-layer methods, where an outer (inviscid dynamic wave) and inner (viscous diffusive wave) solutions are matched. This conceptual model was compared with experiments, and a fair agreement was noted [14]. It was recently compared with 3D computational results based on the RANS equations [16]. This model is a simplified analytical solution of the Saint Venant equations, and, thus, it is of interest to compare it with the general solution of the Saint Venant equations. Given that an exact analytical solution of Saint Venant equations for the dam break wave with boundary friction is so far unknown, it is necessary to compare Whitham's boundary layer type conceptual model with the numerical solution of the Saint Venant equations for the viscous dynamic wave.

As regards to the negative wave, Dressler [17] and Lauber [10] found experimentally that the negative front propagates much faster than predicted by Ritter's theory, with a free surface profile implying strong negative curvatures, and largely deviating from a parabolic shape, during the initial instants following the instantaneous dam break. Dressler [17] and Lauber and Hager [15] linked these strong differences to the existence of severe vertical accelerations. To date, this hypothesis was not verified, except in the near-vicinity of the wall [4]. In order to account for these features, it is necessary to introduce vertical accelerations and non-hydrostatic pressures in a depth-averaged model via use of the vertical momentum balance [18, 19]. However, the negative front propagation celerity remains so far un-analyzed by using a depth-averaged flow model including vertical accelerations.

Given the conceptual importance of Ritter's dam break idealized structure, the need to predict accurately the positive and negative front propagation, and the discrepancies observed experimentally, the specific objectives of this work are:

1. Testing the Whitham/Dressler/Chanson [11, 12, 14] conceptual model for the dry-bed dam break flow problem. To address this objective, the comparison of this simplified analytical model with the full solution of Saint-Venant equations, is conducted. For this task, two accurate numerical solutions of the Saint-Venant equations are produced for reference, using the MUSCL-Hancock finite volume method, and the discontinuous Galerkin finite element method.
2. Detailing the rarefaction wave propagation by including vertical accelerations in a depth-averaged model. To address this objective, vertical accelerations are accounted for by using the Serre-Green-Naghdi equations for weakly-dispersive and fully non-linear water waves, which are a generalization of Saint-Venant equations. The equations are solved by using a hybrid finite volume-finite difference model.

These objectives are systematically developed in the next sections.

## 2 Shallow flow approximations

### 2.1 Dynamic wave with friction effects

A detailed solution of the viscous dynamic wave model is necessary to test the approximate analytical solution composed of a diffusive wave model matched to a inviscid dynamic wave, corresponding to Ritter's model [14]. In this section, two independent numerical models were implement to produce an accurate reference solution of Saint Venant equations with friction effects.

#### 2.1.1 Finite volume method

Equations (1)-(2) are written in conservative vector form, including the flow resistance force, as [5]

$$\frac{\partial \mathbf{U}}{\partial t} + \frac{\partial \mathbf{F}}{\partial x} = \mathbf{S}. \quad (5)$$

Here  $\mathbf{U}$  is the vector of conserved variables,  $\mathbf{F}$  is the flux vector and  $\mathbf{S}$  the source term vector, given by

$$\mathbf{U} = \begin{bmatrix} h \\ hU \end{bmatrix}, \quad \mathbf{F} = \begin{bmatrix} q \\ F \end{bmatrix} = \begin{bmatrix} hU \\ hU^2 + \frac{1}{2}gh^2 \end{bmatrix}, \quad \mathbf{S} = \begin{bmatrix} 0 \\ -ghS_f \end{bmatrix}. \quad (6)$$

Shock capturing finite volume solutions of Eq.(6) using the Godunov upwind method, assisted by robust Riemann solvers (approximate or exact), produce accurate solutions of shallow-water flows [5, 20]. The integral form of Eq.(6) over a control volume in the  $x$ - $t$  plane is [5, 9]

$$\int_t^{t+\Delta t} \int_{x_{i-1/2}}^{x_{i+1/2}} \frac{\partial \mathbf{U}}{\partial t} dxdt + \left( \int_t^{t+\Delta t} \mathbf{F} dt \right)_{i+1/2} - \left( \int_t^{t+\Delta t} \mathbf{F} dt \right)_{i-1/2} = \int_t^{t+\Delta t} \int_{x_{i-1/2}}^{x_{i+1/2}} \mathbf{S} dxdt. \quad (7)$$

To solve Eq. (7) a splitting approach is used. First, the inviscid flow problem, corresponding to the integral solution of the homogeneous system

$$\frac{\partial \mathbf{U}}{\partial t} + \frac{\partial \mathbf{F}}{\partial x} = \mathbf{0}, \quad (8)$$

is tackled. For a rectangular control volume in the  $x$ - $t$  plane, Eq.(7) reads [5]

$$\tilde{\mathbf{U}}_i^{k+1} = \mathbf{U}_i^k - \frac{\Delta t}{\Delta x} (\mathbf{F}_{i+1/2} - \mathbf{F}_{i-1/2}), \quad (9)$$

which is used to update the vector  $\mathbf{U}$ . Here  $\Delta t$  and  $\Delta x$  are the step sizes in the  $x$  and  $t$  axes, respectively,  $k$  refers to the time level,  $i$  is the cell index in the  $x$ -direction, and  $\mathbf{F}_{i+1/2}$  is the numerical flux crossing the interface between cells  $i$  and  $i+1$  (Fig. 3). In this work the MUSCL-Hancock method is used to solve Eq. (9) [5, 9], which is second-order accurate in both space and time. The solution process starts with the cell-averaged values of conserved variables at time level  $k$ ,  $\mathbf{U}_i^k$ . For second order space accuracy, a piecewise linear reconstruction is conducted within each cell [5] (Fig. 3). Linear slopes resulting from the reconstructed solution must be limited to avoid spurious oscillations near discontinuities. Let letters  $L$  and  $R$  denote the reconstructed variables at the left and right sides of a cell interface, the resulting values of  $\mathbf{U}$  at each of its sides are

$$\mathbf{U}_{i+1/2}^L = \mathbf{U}_i^k + \frac{1}{2} \Phi_{i-1/2}^+ (\mathbf{U}_i^k - \mathbf{U}_{i-1}^k); \quad \mathbf{U}_{i+1/2}^R = \mathbf{U}_{i+1}^k - \frac{1}{2} \Phi_{i+3/2}^- (\mathbf{U}_{i+2}^k - \mathbf{U}_{i+1}^k), \quad (10)$$

with  $\Phi_{i-1/2}^+$  and  $\Phi_{i+3/2}^-$  as diagonal limiter matrices [5]. The Minmod limiter is used in this work. In the MUSCL-Hancock method, an evolution of boundary extrapolated values  $\mathbf{U}_{i+1/2}^L$  and  $\mathbf{U}_{i+1/2}^R$  at interface  $i+1/2$  over half the time step is conducted to regain second order accuracy in time. Based on a Taylor series expansion in space and time, interface values are then given by [5]



$$\begin{aligned}\bar{\mathbf{U}}_{i+1/2}^L &= \mathbf{U}_{i+1/2}^L - \frac{\Delta t}{2\Delta x} \left[ \mathbf{F}(\mathbf{U}_{i+1/2}^L) - \mathbf{F}(\mathbf{U}_{i-1/2}^R) \right], \\ \bar{\mathbf{U}}_{i+1/2}^R &= \mathbf{U}_{i+1/2}^R - \frac{\Delta t}{2\Delta x} \left[ \mathbf{F}(\mathbf{U}_{i+3/2}^L) - \mathbf{F}(\mathbf{U}_{i+1/2}^R) \right].\end{aligned}\quad (11)$$

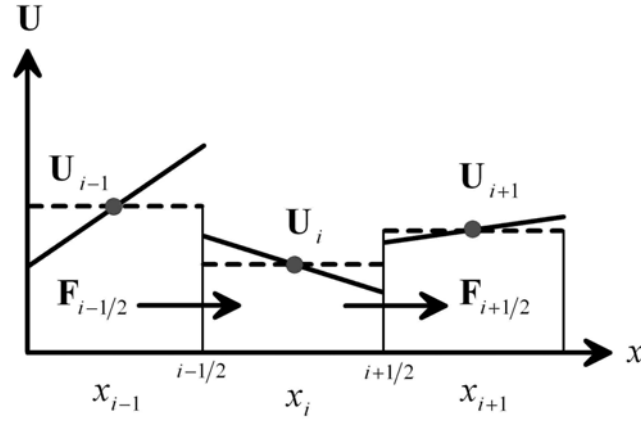


Figure 3 Finite volume discretization

With these evolved boundary extrapolated variables  $\bar{\mathbf{U}}_{i+1/2}^L$  and  $\bar{\mathbf{U}}_{i+1/2}^R$  defining states  $L$  and  $R$ , the numerical flux is computed using the HLL approximate Riemann solver as [5]

$$\mathbf{F}_{i+1/2} = \begin{cases} \mathbf{F}_L & \text{if } S_L \geq 0 \\ \frac{S_R \mathbf{F}_L - S_L \mathbf{F}_R + S_R S_L (\mathbf{U}_R - \mathbf{U}_L)}{S_R - S_L}, & \text{if } S_L \leq 0 \leq S_R \\ \mathbf{F}_R & \text{if } S_R \leq 0 \end{cases} \quad (12)$$

Here  $\mathbf{F}_L$  and  $\mathbf{F}_R$  are the fluxes computed at states  $L$  and  $R$ . Robust wave speeds estimates  $S_L$  and  $S_R$  for a wet bed are given by [5]

$$S_L = U_L - a_L q_L, \quad S_R = U_R + a_R q_R, \quad (13)$$

where  $a = (gh)^{1/2}$ , and  $q_K (K = L, R)$  is

$$q_K = \begin{cases} \left[ \frac{1}{2} \left( \frac{h_*(h_* + h_K)}{h_K^2} \right) \right]^{1/2} & h_* > h_K \\ 1 & h_* \leq h_K \end{cases} \quad (14)$$

The flow depth at the star region of the Riemann problem at each interface  $h_*$  is [5]

$$h_* = \frac{1}{g} \left( \frac{1}{2} (a_L + a_R) + \frac{1}{4} (U_L - U_R) \right)^2. \quad (15)$$

For the dry-bed problem, the celerity of the signals are given by

$$S_L = U_R - 2a_R \text{ (if } h_L = 0 \text{)}, S_R = U_L + 2a_L \text{ (if } h_R = 0 \text{)}. \quad (16)$$

Once Eq. (9) is applied, the effect of the source terms is introduced by solving the ODE [5]

$$\frac{d\mathbf{U}}{dt} = \mathbf{S}. \quad (17)$$

Given that the only source term in Eq. (17) is the resistance force appearing in the momentum equation, it is reduced to the scalar ODE

$$\frac{dq}{dt} = -\frac{f}{8} U^2, \quad (18)$$

where  $f$  is the Darcy-Weisbach friction factor. Equation (18) is discretized implicitly, resulting in the algebraic expression

$$U_i^{k+1} = \frac{\tilde{q}_i^k}{h_i^{k+1}} - \Delta t \frac{f}{8h_i^{k+1}} (U_i^{k+1})^2. \quad (19)$$

Equation (19) is a quadratic equation that is solved each time step to obtain the cell-averaged velocity  $U_i^{k+1}$  accounting for the friction effects. In this work, a threshold value of  $10^{-8}$  is used to identify dry cells. If the water depth is negative at a cell after the evolution of conserved variables, the vector  $\mathbf{U}$  is set to zero. If the water depth falls below the threshold value, the velocity is set to zero. For stability in time of the explicit scheme, the Courant-Friedrichs-Lewy number CFL must be less than unity [5]. Given the value of CFL,  $\Delta t$  is determined at time level  $k$  from

$$\Delta t = \text{CFL} \left[ \frac{\Delta x}{\max_i \left| U_i^k + (gh_i^k)^{1/2} \right|} \right]. \quad (20)$$

In Fig. 4 the experiments by Schoklitsch [21] for a dam break wave in a dry, rectangular, horizontal flume are considered as test case. The flume is 0.093 m in width, 0.08 m in height, and 20 m in length. The dam was located at coordinate  $x = 10$  m, and the removal was considered instantaneous. The tailwater portion of the flume was initially dry, and the water depth in the dam 0.074 m. Experimental measurements conducted by Schoklitsch [21] for two times after removal of the dam, namely  $t = 3.75$  s and  $t = 9.4$  s, are plotted in Fig. 4a and 4b, respectively. The predictions using the finite volume model were conducted adopting  $f = 0.03$  [14], resulting in a good agreement with observations, as depicted in Fig. 4. The numerical solution was conducted using 700 cells and CFL = 0.1 to produce accurate results, despite stable results were feasible with CFL = 0.9 and half of the cells. The effect of flow resistance in this test was significant, as observed from the deviation of Ritter's solution in the same figure.



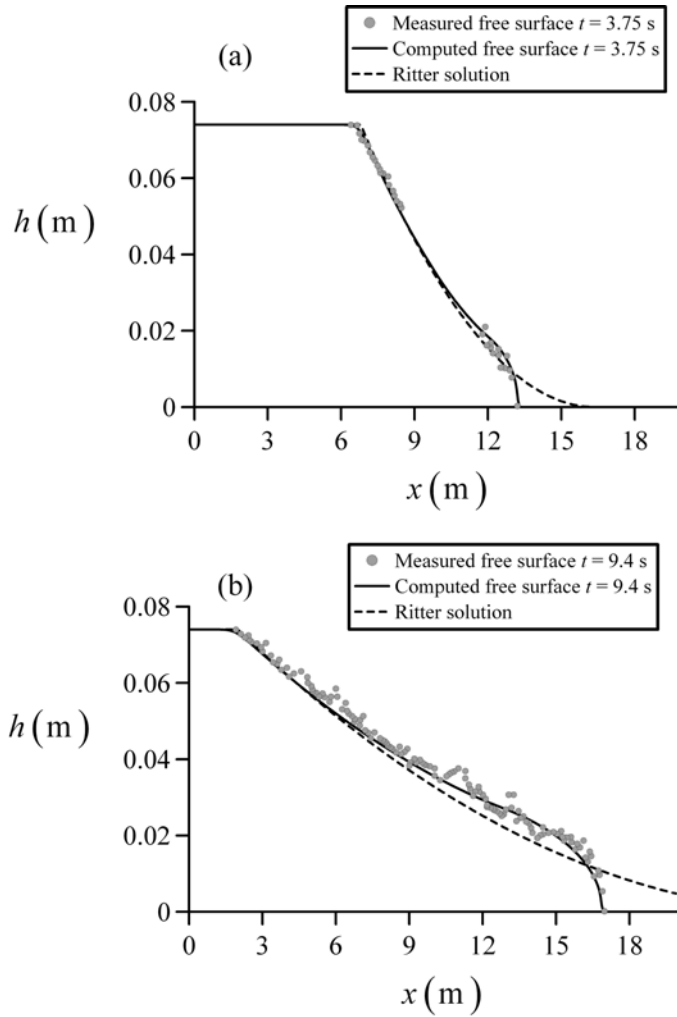


Figure 4 Dry-bed dam break wave test case: Comparison of computed and measured [21] instantaneous free surface profiles

### 2.1.2 Discontinuous Galerkin finite element method

An alternative solution to the dynamic wave model may be developed using the discontinuous Galerkin method (DGM) [7, 22]. The computational domain is divided in a number of finite elements, and the value of  $\mathbf{U}$  at the common interface of two adjacent elements is allowed to be discontinuous (Fig. 5a). Within a generic element "e" the solution  $\mathbf{U}(x, t)$  is approximated by the interpolation function

$$\mathbf{U}(x, t) \approx \hat{\mathbf{U}} = \sum_{j=1}^2 \mathbf{N}_j(x) \mathbf{U}_j(t), \quad (21)$$

where  $\mathbf{U}_j$  are the nodal values of  $\mathbf{U}$  at the boundaries of each element ( $j = 1$  for left node and  $j = 2$  for right node). At a node, shared by two adjacent elements,  $\mathbf{U}$  has two different values at its left- and right-sides. Basically, this produces a number of local Riemann problems at the interfaces of elements. The shape functions  $\mathbf{N}_j(x)$  are, in local normalized coordinates  $\xi$  of an element (Fig. 5b),

$$N_1 = 0.5(1 - \xi), \quad N_2 = 0.5(1 + \xi). \quad (22)$$

In the discontinuous Galerkin method, the test functions are taken equal to the shape or interpolating functions. Thus, Eq. (5) is multiplied by  $\mathbf{N}_i$  (with  $i = 1$  and 2), and integrated over an element, resulting [7]

$$\int_{x_{e-1/2}}^{x_{e+1/2}} \mathbf{N}_i \frac{\partial \mathbf{U}}{\partial t} dx + \int_{x_{e-1/2}}^{x_{e+1/2}} \mathbf{N}_i \frac{\partial \mathbf{F}}{\partial x} dx = \int_{x_{e-1/2}}^{x_{e+1/2}} \mathbf{N}_i \mathbf{S} dx. \quad (23)$$

Integrating Eq. (23) by parts, and substituting the predictor of  $\mathbf{U}(x, t)$  within the element, given by Eq. (21), produces [7]

$$\int_{x_{e-1/2}}^{x_{e+1/2}} \mathbf{N}_i \left[ \sum_{j=1}^2 \mathbf{N}_j \frac{\partial \mathbf{U}_j}{\partial t} \right] dx + \mathbf{N}_i (\mathbf{F}_{e+1/2} - \mathbf{F}_{e-1/2}) - \int_{x_{e-1/2}}^{x_{e+1/2}} \frac{\partial \mathbf{N}_i}{\partial x} \hat{\mathbf{F}} dx = \int_{x_{e-1/2}}^{x_{e+1/2}} \mathbf{N}_i \hat{\mathbf{S}} dx, \quad (24)$$

where

$$\mathbf{F}(\mathbf{U}) \approx \hat{\mathbf{F}}(\mathbf{U}) = \mathbf{F}(\hat{\mathbf{U}}), \quad \mathbf{S}(\mathbf{U}) \approx \hat{\mathbf{S}}(\mathbf{U}) = \mathbf{S}(\hat{\mathbf{U}}). \quad (25)$$

Equation (24) is the basic relation of the DGM. Equation (24) yields for the discretized continuity equation a system of two equations to determine the evolution of the water depths ( $h_1, h_2$ ) at each node of the element, namely [7]

$$\Delta x \begin{bmatrix} 2/6 & 1/6 \\ 1/6 & 2/6 \end{bmatrix} \frac{\partial}{\partial t} \begin{bmatrix} h_1 \\ h_2 \end{bmatrix} + \begin{bmatrix} -q_{e-1/2} \\ q_{e+1/2} \end{bmatrix} - \begin{bmatrix} -0.5 & -0.5 \\ 0.5 & 0.5 \end{bmatrix} \begin{bmatrix} q_1 \\ q_2 \end{bmatrix} = \begin{bmatrix} 0 \\ 0 \end{bmatrix}. \quad (26)$$

Likewise, from Eq. (24) the evolution of discharge at the nodes of the element ( $q_1, q_2$ ) is given by the system [7]

$$\Delta x \begin{bmatrix} 2/6 & 1/6 \\ 1/6 & 2/6 \end{bmatrix} \frac{\partial}{\partial t} \begin{bmatrix} q_1 \\ q_2 \end{bmatrix} + \begin{bmatrix} -F_{e-1/2} \\ F_{e+1/2} \end{bmatrix} - \int_{-1}^1 \frac{\partial N_i}{\partial \xi} \hat{F} d\xi = -\frac{\Delta x}{2} \int_{-1}^1 N_i g h \hat{S}_f d\xi, \quad (27)$$

where the integrals were transformed from the global  $x$ -coordinate to the local element coordinate  $\xi$  [7].

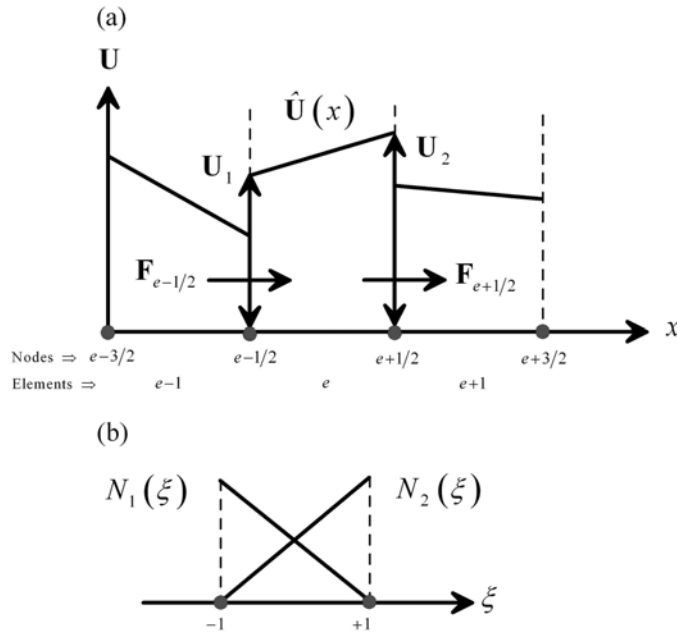


Figure 5 Finite element discretization

The numerical flux  $\mathbf{F}_{e+1/2}$  at the common interface of two adjacent finite elements (Fig. 5a) is computed solving a local Riemann problem by using the HLL approximate Riemann solver, already described for the finite volume solver. The slope of the solution within an element, determined by the actual values of  $\mathbf{U}_1$  and  $\mathbf{U}_2$ , must be limited to avoid unphysical oscillations near shocks, but preserving the corresponding element-averaged values [7]. Here, the minmod limiter is used. The space integrals are evaluated by a two-point Gaussian quadrature formula, using the identities stated in Eq. (25). A friction factor  $f = 0.03$  is used in the simulations. Once numerical fluxes at element

boundaries and space integrals along the element are evaluated, based on the known information at the actual time level  $k$ , Eqs. (26) and (27) are used to evolve in time  $h_1$ ,  $h_2$ ,  $q_1$  and  $q_2$  by resort to a one-step forward Euler method.

The solution for the dam break propagation on a dry bed previously presented in Fig. 4 is further considered in Fig. 6, where the results of the DGM, produced using 700 elements and  $CFL = 0.1$ , are compared with the former results of the finite volume method, for both  $h(x, t)$  and  $q(x, t)$ . For the DGM, the maximum CFL for stability is  $1/3$  [7]. To have a meaningful comparison of the DGM method and the finite volume method, both models are solved with identical CFL and spatial divisions of the domain, therefore. It can be observed that results of both techniques are in excellent agreement. It is not claimed that the discontinuous Galerkin method is more precise than the MUSCL-Hancock finite volume method, or vice-versa; Simply, two accurate methods to solve the Saint-Venant equations are used in this work to produce a solution to a problem where an exact analytical solution is unknown, namely the viscous dam break wave. Both methods excellently agree, thereby confirming the accuracy of the numerical solution produced. Such high quality reference solution is necessary to undertake a precise evaluation of the simplified analytical solution based on the Whitham/Dressler/Chanson boundary-layer type conceptual model [11, 12, 14]. Given that both numerical solutions excellently agree, in the rest of the work only the results corresponding to the finite volume method are presented.

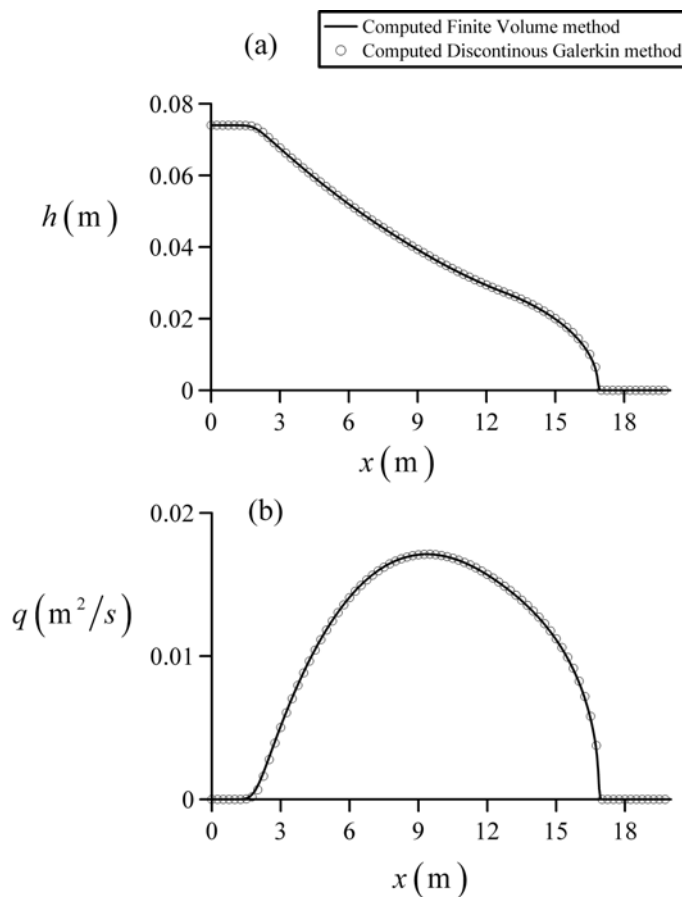


Figure 6 Comparison of finite volume method and DGM for the viscous dam break wave

## 2.2 Boundary-layer analytical solution

Whitham, Dressler and Chanson [11, 12, 14] conceptualized the computation of the dam break flow over a dry bed using boundary layer arguments. Near the dry bed front, they argued that frictional resistance controls the motion, which is assumed to be not accelerated. Then, of necessity, an exact

balancing of friction and hydrostatic forces must be preserved. Basically, these are the conditions of the so-called diffusive wave, obtained from the momentum balance contained in Eq. (5) as

$$\frac{\partial h}{\partial x} = -\frac{f}{8} \frac{U^2}{gh}. \quad (28)$$

At an undermined point away from the dry-bed front, frictional forces are negligible, but accelerations (local and convective) are then significant. The conceptual model proposed was therefore made up of a composite wave solution matching Eq. (28) to Ritter's solution for the inviscid dynamic wave. The matching point is determined forcing conservation of the water volume initially at rest in the reservoir [14]. This model was briefly presented by Dressler [17] and extensively developed by Chanson [14]. As additional hypothesis, it was assumed that the velocity in the tip wave portion is not largely varying in space, that is,  $U(x, t) \approx U_F(t)$ , which is, thus, the dry-front celerity. Analytical integration of Eq. (28) between an arbitrary point and the dry-front, where  $x = x_F$  and  $h = 0$ , produce [12, 14, 17]

$$h(x, t) = -\left[ \frac{f}{4} \frac{U_F^2}{g} (x_F - x) \right]^{1/2}. \quad (29)$$

Curiously, we remark here that Whitham [12] discarded Eq. (29), which he considered inaccurate without giving evidence. However, both Dressler [17] and Chanson [14] found elements in favor of it. Thus, a detailed comparison of this simplified analytical solution with the detailed numerical solution of Saint-Venant equations is presented as follows. The dimensionless dry-front celerity is given, based on mass conservation, by the identity [14]

$$\frac{8}{3} \frac{1}{f} \frac{\left(1 - \frac{1}{2}\theta\right)^3}{\theta} = T, \quad (30)$$

where the normalized time is  $T = t(g/h_o)^{1/2}$  and the dimensionless front celerity is  $\theta = U_F/(gh_o)^{1/2}$ . Equation (30) gives the function  $\theta = \theta(T)$  upon numerical solution. The assembling point  $x_e$  of the inner (viscous diffusive wave) and outer (inviscid dynamic wave) solutions is given by [14]

$$X_e = \left(\frac{3}{2}\theta - 1\right)T, \quad (31)$$

where  $X_e = x_e/h_o$ , and the dry-front position is [14]

$$X_F = \left(\frac{3}{2}\theta - 1\right)T + \frac{4}{f\theta^2} \left(1 - \frac{1}{2}\theta\right)^4. \quad (32)$$

The free surface profile up- and downstream of  $x_e$  is determined from Eqs. (3) and (29), respectively. Likewise, upstream of  $x_e$  the velocity profile is given by Ritter's Eq. (4), reaching the constant value  $U_F$  along the tip portion.

Computations using the analytical model were conducted as follows. First, Eq. (30) was numerically solved for a given instant  $T$  using a Newton-Raphson algorithm [23] to get the corresponding value of  $\theta$ . Second, Eqs. (31) and (32) were used to determine the boundaries of the tip portion, where Eq. (29) gives the free surface profile. Upstream from  $x_e$  Ritter's solution was applied. The finite volume numerical results previously presented in Fig. 4 for  $t = 9.4$  s are plotted again in Fig. 7 to evaluate the analytical results.

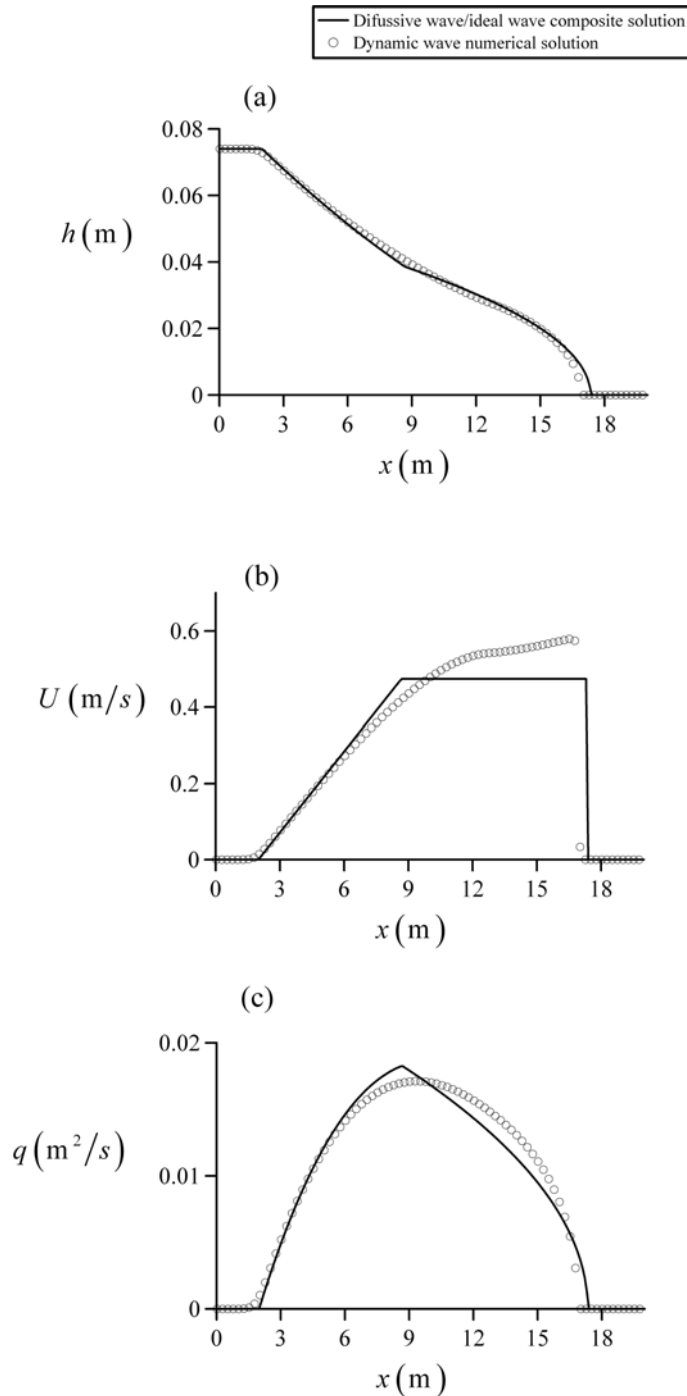


Figure 7 Comparison of the numerical solution of the dynamic wave with the simplified boundary-layer type analytical solution

The analytical solution for the water depth, velocity and discharge is presented in the same figure. It can be observed that the analytical water depth prediction is very close to the numerical solution (Fig. 7a), despite the visible slope break at the assembling point of the inviscid dynamic wave and the viscous diffusive wave. Velocity profiles are compared in Fig. 7b. As expected, the constant velocity profile in the tip portion is only an approximation, given that the numerically-computed velocity profiles also increase in this domain, in agreement with Lauber's [10] experimental observations. However, the dry-bed front position is adequately predicted by the analytical model (Fig. 7b), giving evidence of the accuracy of the dry-front celerity prediction. The numerical and analytical discharges are compared in Fig. 7c, where a fair agreement is noted. Notably, the

approximation of the velocity profile in the tip zone provokes some deviations from the numerical solution, but, overall, the simplified analytical solution gives a reasonable estimate of the discharge.

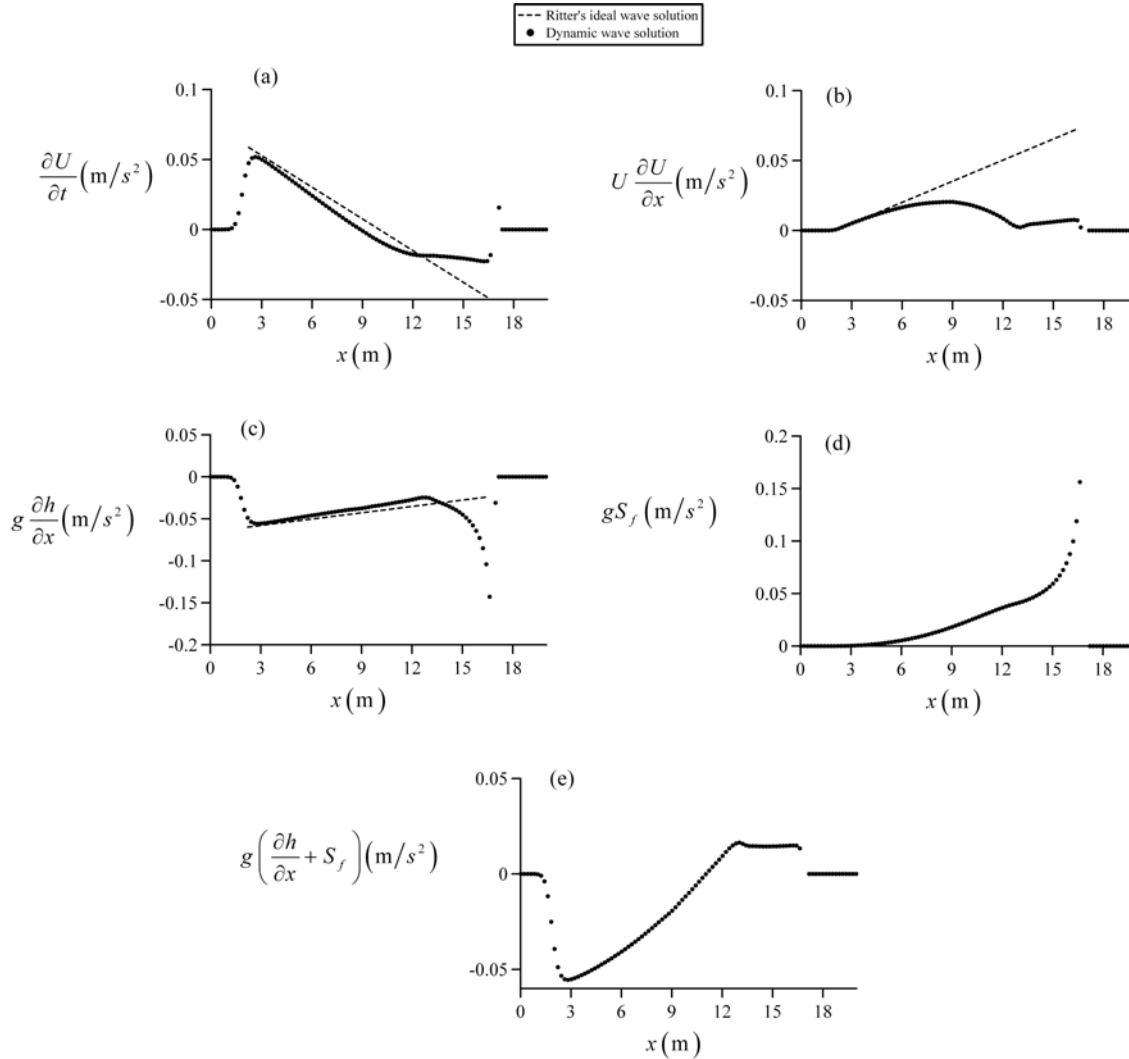


Figure 8 Momentum balance terms along the viscous dam break wave (dam wall coordinate at  $x = 10$  m)

The momentum balance written in primitive or non-conservative variables ( $h$ ,  $U$ ) is [5, 14]

$$\frac{\partial U}{\partial t} + U \frac{\partial U}{\partial x} + g \frac{\partial h}{\partial x} + gS_f = 0. \quad (33)$$

The terms with spatial derivatives in Eq. (33) were discretized using second-order accurate central finite differences, and the time derivative using a forward finite difference. The discretized derivatives were evaluated using the numerical solution produced using the finite-volume method. The results are displayed in Fig. 8. The numerically-computed local and convective accelerations are compared with those obtainable from Ritter's inviscid solution, namely,

$$\frac{\partial U}{\partial t} = -\frac{2}{3} \frac{x}{t^2}, \quad (34)$$

and

$$U \frac{\partial U}{\partial x} = \frac{4}{9t} \left[ (gh_o)^{1/2} + \frac{x}{t} \right], \quad (35)$$

respectively. Further, the pressure force gradient was also determined from the inviscid solution, resulting



$$g \frac{\partial h}{\partial x} = -\frac{2}{9t} \left[ 2(gh_o)^{1/2} - \frac{x}{t} \right]. \quad (36)$$

A fact that deserves consideration on inspecting Eqs. (34)-(36) is that the local acceleration exactly balances the sum of the convective acceleration plus the pressure force gradient. It implies that the unsteady dam break wave is largely governed by local acceleration effects, a matter rarely emphasized. It is instructive to look how the flow resistance modifies this structure existing in the inviscid dynamic wave. As revealed in Fig. 8, away from the tip portion the inviscid dynamic wave is a very good approximation. Local and convective accelerations are little affected by friction (Fig. 8 a, b). Approaching the dry-bed front, the friction force increases, as also does the pressure force gradient given that the water surface slope becomes steeper (Fig. 8 c, d). According to Whitham [12], one would expect an exact balancing of the pressure and resistance forces. As indicated by the numerical results in Fig. 8e, this is in fact a very good approximation, but not exact; convective accelerations can be ignored near the dry front, but the magnitude of  $\partial U/\partial t$ , tough small, cannot be ignored at first glance. Its magnitude near the dry front is about 15% of the resistive force. However, despite the diffusive wave assumption is not exactly verified, the water surface predictions of this model are in fact very good.

### 3 Wave solution accounting for vertical accelerations

In this section the viscous dam break wave is simulated using a depth-averaged model where the vertical acceleration effects are introduced, namely the Serre-Green-Naghdi equations.

#### 3.1 Serre-Green-Naghdi equations for fully non-linear and weakly dispersive water waves

Serre [24] derived equations for weakly-dispersive, fully non-linear water waves by depth-averaging of the mass and momentum conservation equations, resulting the system

$$\frac{\partial h}{\partial t} + \frac{\partial(Uh)}{\partial x} = 0, \quad (37)$$

$$\frac{\partial(Uh)}{\partial t} + \frac{\partial}{\partial x} \left[ g \frac{h^2}{2} + U^2 h + \underbrace{\left( U_x^2 - UU_{xx} - U_{xt} \right) \frac{h^3}{3}}_{\text{Effect of vertical acceleration for an inviscid fluid}} \right] = -ghS_f. \quad (38)$$

To obtain these equations, Serre [24] assumed that the velocity in the  $x$ -direction is uniform with depth and equal to its depth-averaged value  $U = q/h$ . The compatible vertical velocity component resulted to be linearly distributed with depth. By introducing these velocity components in an inviscid vertical momentum balance, obtained from the corresponding Euler equation, the effect of the vertical acceleration was accounted for into the depth-averaged  $x$ -momentum balance [see term under-braced in Eq. (38), where  $U_x = \partial U/\partial x$ ,  $U_{xx} = \partial^2 U/\partial x^2$  and  $U_{xt} = \partial^2 U/\partial x \partial t$ ]. Equation (38) was obtained by Shu and Gardner [25] and Green and Naghdi [26, 27] by applying the irrotational flow theory. The system is called the *Serre-Green-Naghdi* equations in coastal engineering, despite in civil and environmental engineering these are named as *Serre* equations [28], or simply *Boussinesq* equations [29]. These equations are discussed in depth by Barthelemy [30], Cienfuegos et al. [31], Dias and Milewski [32], and Bonneton et al. [33], where numerical solutions of coastal engineering problems are addressed, including solitary wave propagation. Castro-Ortiz and Chanson [34] applied the steady-state version of Eqs. (37)-(38) to model near-critical flows, like undular hydraulic jumps. Here, we focus on their application to Ritter's dam break problem.

For a dam break wave propagating over an initially wet bed, the inviscid acceleration term introduced into Eq. (38) produces undulations in the shock front [28, 29, 35, 36]. These undulations

are not attenuated as the wave evolves in time, given that a drawback of Eq. (38) is that wave breaking and turbulence effects are not accounted for. It is well-known experimentally that undulations on the shock are formed if the ratio of downstream to upstream initial water depths in the dam is above 0.4 [35, 36]. For smaller ratios, turbulence produce wave breaking and the undulations are progressively suppressed, until no wave trains are finally observed for a dry-bed dam break flow wave. Vertical accelerations are very strong at the initial stages of dam break waves [13, 37, 38], but turbulence and wave breaking are dominant features [13]. If dam break wave simulations are conducted using Eqs. (37)-(38), undulations at the shock front generated by the inviscid acceleration term are produced even for ratios of tailwater to upstream depth below 0.4. Thus, for a realistic prediction of dam break waves based on Eqs. (37)-(38) turbulence effects must be accounted for. Hosoda and Tada [39] and Hosoda et al. [40] proposed a simple correction to Eq. (38), where turbulence effects are accounted for introducing a damping factor  $\varepsilon$  as

$$\frac{\partial(Uh)}{\partial t} + \frac{\partial}{\partial x} \left[ g \frac{h^2}{2} + U^2 h + \varepsilon (U_x^2 - UU_{xx} - U_{xt}) \frac{h^3}{3} \right] = -ghS_f. \quad (39)$$

This parameter is used to model the turbulence reduction of the inviscid vertical acceleration effects in the  $x$ -momentum balance. The parametrization proposed by Hosoda and Tada [39] is based on the assumption that if the non-hydrostatic inviscid terms are not important, then the results from the Serre equations should collapse with those from the Saint-Venant equations. Basically, it implies that under the action of turbulence the vertical momentum balance of an inviscid fluid is damped, approaching a hydrostatic vertical momentum balance as turbulence intensity increases. Thus, the energy dissipation due to wave breaking is assumed to be adequately accounted for by the Rankine-Hugoniot jump conditions across moving shocks [5, 41]. Hosoda and Tada [39] and Hosoda et al. [40] proposed a damping factor  $\varepsilon$  that gradually attenuates the non-hydrostatic term under the action of turbulence using the solitary wave as conceptual model (Appendix I). If a branch of the solitary wave profile is assumed to describe the first wave of an undular shock front, wave breaking of a solitary wave may be linked to the wave breaking at the undular shock. Based on undular bore experimental data, the limiting supercritical Froude number for wave breaking of an undular shock is adopted to be  $F_1 = 1.25$  [39, 40]. Thus, if the solitary wave breaks at this value of  $F_1$ , the maximum water surface slope on the upstream branch of the solitary wave profile is located at the inflection point, with a value, upon using the solitary wave profile function [40],

$$\left| \frac{\partial h}{\partial x} \right|_{cr} = 0.225. \quad (40)$$

This slope is adopted as a threshold value above which wave breaking occurs due to the action of turbulence. Hosoda and Tada [39] proposed the factor  $\varepsilon$

$$\varepsilon = \begin{cases} \exp \left[ -\varsigma \left( \left| \frac{\partial h}{\partial x} \right| - \left| \frac{\partial h}{\partial x} \right|_{cr} \right) \right] & \text{if } \left| \frac{\partial h}{\partial x} \right| > \left| \frac{\partial h}{\partial x} \right|_{cr}, \\ 1 & \text{else} \end{cases} \quad (41)$$

that gradually introduces the damping effect of turbulence on the vertical acceleration, depending on the local free surface slope. Comparison with laboratory data of undular hydraulic jumps indicates a calibration parameter  $\varsigma = 2$  [39]. The friction slope  $S_f$  is determined using Darcy-Weisbach equation.

### 3.2 Computation of the wave profile

The system of Eqs. (37) and (39) is solved here using a finite volume-finite difference method. Boussinesq-type water wave propagation models are extensively solved in the coastal engineering literature using 4<sup>th</sup>-order accurate schemes in space and time [31, 41, 42, 43, 44]. The reason underlying this practice is that truncation errors originating from the discretization to second-order

accuracy of Saint-Venant type leading terms can induce numerical dispersion. This problem is serious for large scale simulations using sparse time-space meshes [42]. However, if a fine mesh is used in second-order accurate schemes this effect disappears, rendering the model a simple and useful tool. It is not infrequent to find unsteady non-hydrostatic models solved using second-order accurate schemes [19, 39, 45, 46], or even of first-order [47], producing very good results. For the basic test cases conducted here, a second-order accurate model in space and time was implemented based on the previously described MUSCL-Hancock scheme. After some mathematical manipulation, using Eq. (37) and treating  $\varepsilon$  as independent of  $x$ , Eq. (39) can be rewritten in the convenient form

$$\underbrace{\frac{\partial}{\partial t} \left[ Uh - \frac{\partial}{\partial x} \left( \varepsilon U_x \frac{h^3}{3} \right) \right]}_{\text{collected term for time-stepping}} + \underbrace{\frac{\partial}{\partial x} \left[ g \frac{h^2}{2} + U^2 h \right]}_{\text{Saint-Venant flux term}} = - \underbrace{ghS_f}_{\text{flow resistance term}} + \underbrace{\frac{\partial}{\partial x} \left[ \varepsilon (UU_{xx} - U_x^2) \frac{h^3}{3} + \varepsilon U_x q_x h^2 \right]}_{\text{non-hydrostatic source term}} \quad (42)$$

where all time derivatives are collected in a single time-stepping term, and convective contributions originating from non-hydrostatic pressures are treated as a source term. Thus, the one-dimensional system of conservation laws to be solved is

$$\frac{\partial \mathbf{W}}{\partial t} + \frac{\partial \mathbf{F}}{\partial x} = \mathbf{Z}, \quad (43)$$

where

$$\mathbf{W} = \begin{bmatrix} h \\ \sigma \end{bmatrix} = \begin{bmatrix} h \\ hU - \varepsilon \frac{h^3}{3} U_{xx} - \varepsilon h^2 h_x U_x \end{bmatrix}, \quad \mathbf{F} = \begin{bmatrix} q \\ F \end{bmatrix} = \begin{bmatrix} hU \\ hU^2 + \frac{1}{2} gh^2 \end{bmatrix}$$

$$\mathbf{Z} = \begin{bmatrix} 0 \\ -ghS_f + \frac{\partial}{\partial x} \left[ \varepsilon (UU_{xx} - U_x^2) \frac{h^3}{3} + \varepsilon U_x q_x h^2 \right] \end{bmatrix} = \begin{bmatrix} 0 \\ -ghS_f + \Omega \end{bmatrix}. \quad (44)$$

The solution of Eq. (43) was conducted using a finite volume-finite difference method as follows. First, using known values of the variables ( $h$ ,  $q$ ) at time level  $k$ , the numerical flux  $\mathbf{F}_{i+1/2}$  was determined as previously described using the MUSCL-Hancock method with the HLL approximate Riemann solver. This step is identical to the solution of Saint-Venant equations, therefore. Once this computation is done, the water depths at the new time level  $k+1$  are from the finite-volume conservative formula

$$h_i^{k+1} = h_i^k - \frac{\Delta t}{\Delta x} (q_{i+1/2} - q_{i-1/2}), \quad (45)$$

where  $\Delta t$  is determined using Eq. (20). This value of the water depth is then used to evaluate the source term  $\mathbf{Z}$ ; the auxiliary variable  $\sigma$  at the new time level is then from the finite-volume method

$$\sigma_i^{k+1} = \sigma_i^k - \frac{\Delta t}{\Delta x} (F_{i+1/2} - F_{i-1/2}) - \Delta t g h_i^{k+1} S_f(q_i^k, h_i^{k+1}) + \Delta t \Omega(q_i^k, h_i^{k+1}). \quad (46)$$

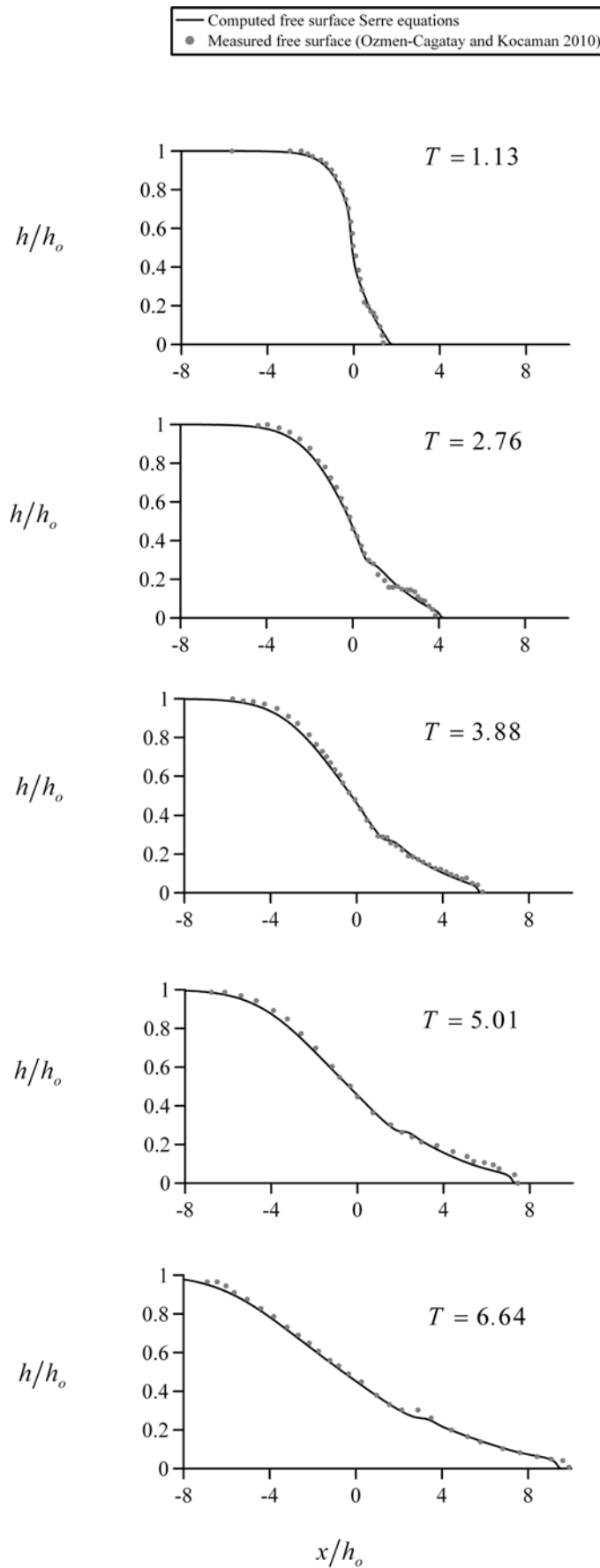
The spatial derivatives in the source term  $\Omega$  are approximated using second-order central finite differences. Once the values of  $\sigma$  are determined at each finite-volume for the new time level, the following elliptic problem is stated at each cell of the computational domain

$$\sigma_i^{k+1} = h_i^{k+1} U_i^{k+1} - \varepsilon_i^k \left( \frac{h^3}{3} \frac{\partial^2 U}{\partial x^2} \right)_i^{k+1} - \varepsilon_i^k \left( h^2 \frac{\partial h}{\partial x} \frac{\partial U}{\partial x} \right)_i^{k+1}. \quad (47)$$

The space derivatives in Eq. (47) are discretized using second-order central finite differences, and the value of  $\varepsilon_i^k$  is determined using Eq. (41). Equation (47) produces an algebraical relation containing the unknown values of the velocity at the new time level for the 3 surrounding cells  $i-1$ ,  $i$  and  $i+1$ . Equation (47) for all  $i$ -cells are assembled, producing a tridiagonal system of equations,

that is easily solved using the Thomas algorithm [23]. Once the velocity  $U_i^{k+1}$  is determined, the cell-averaged discharge  $q_i^{k+1}$  is evaluated.

The prediction of the time evolution of the wave profile using the Serre equations is compared in Fig. 9 with the experimental measurements by Ozmen-Cagatay and Kocaman [48] at different normalized times  $T$  since the gate opening. In these experiments, the gate opening time was between 0.6 and 0.8 s based on image-processing work, and it is considered in fact an instantaneous opening, therefore. The shape of the dam break wave curves presented in Fig. 9 are very similar to those previously measured by Dressler [17]. The upstream water depth in the experiments by Ozmen-Cagatay and Kocaman [48] was  $h_o = 0.25$  m. For the simulation 1300 cells and  $CFL = 0.1$  were used, with a constant friction factor  $f = 0.015$ . It can be observed that the prediction based upon the Serre equations is in good agreement with observations even for very small times since the gate opening, e.g.  $T = 1.13$ . For reference, the same experiments are plotted in Fig. 10 and compared with the parabolic prediction by Ritter [6]. It can be observed that the parabolic shape predicted by Ritter [6] is not in agreement with observations, even for the quite large time  $T = 6.64$ . At this time, the positive wave is in fair agreement with data, but the negative wave is clearly not.



509  
510 Figure 9. Comparison of computed (Serre equations) and measured [48] wave profiles

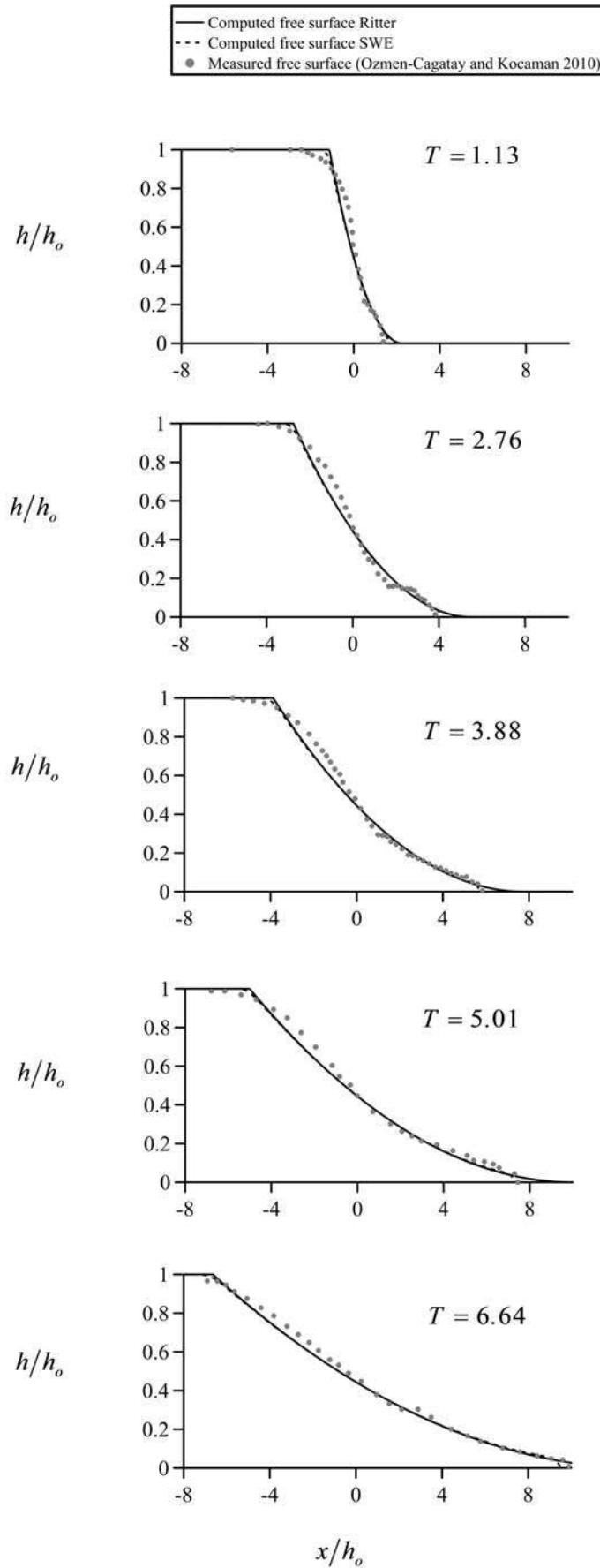


Figure 10. Comparison of analytical solution [6], numerical solution of the shallow-water equations (SWE,  $\varepsilon = 0$ ) and measured [48] wave profiles



The Serre equations solver was run setting  $\varepsilon = 0$  using identical physical and numerical conditions and the results are displayed in Fig. 10. This is the solution of a dynamic wave with friction, which is in excellent agreement with Ritter's solution, but, as expected, deviates from physical data. Notably, none of the wave fronts are correctly predicted by Ritter's approach. In contrast, the Serre equations does a good work tracking the position of the dry and negative wave fronts for all  $T$ . Further, Serre equations correctly predict the shape of the rarefaction wave, implying negative free surface curvature, e.g.  $\partial^2 h / \partial x^2 < 0$ . Thus, the Serre equations produce an improved wave profile prediction as compared to Ritter's parabolic profile, including the tracking of the wave fronts. The celerity of the negative wave predicted by the Serre-Green-Naghdi equations is larger than the theoretical value  $(gh_o)^{1/2}$  predicted by the Saint-Venant equations during the initial instants. This is directly linked to the existence of non-zero vertical acceleration. At later times, however, the celerity of the negative wave decreases toward the asymptotic value predicted by the Saint-Venant equations. This was clearly shown in the recent experiments of Leng and Chanson [49] (Fig. 6 in this paper), as well in the earlier data of Lauber [10].

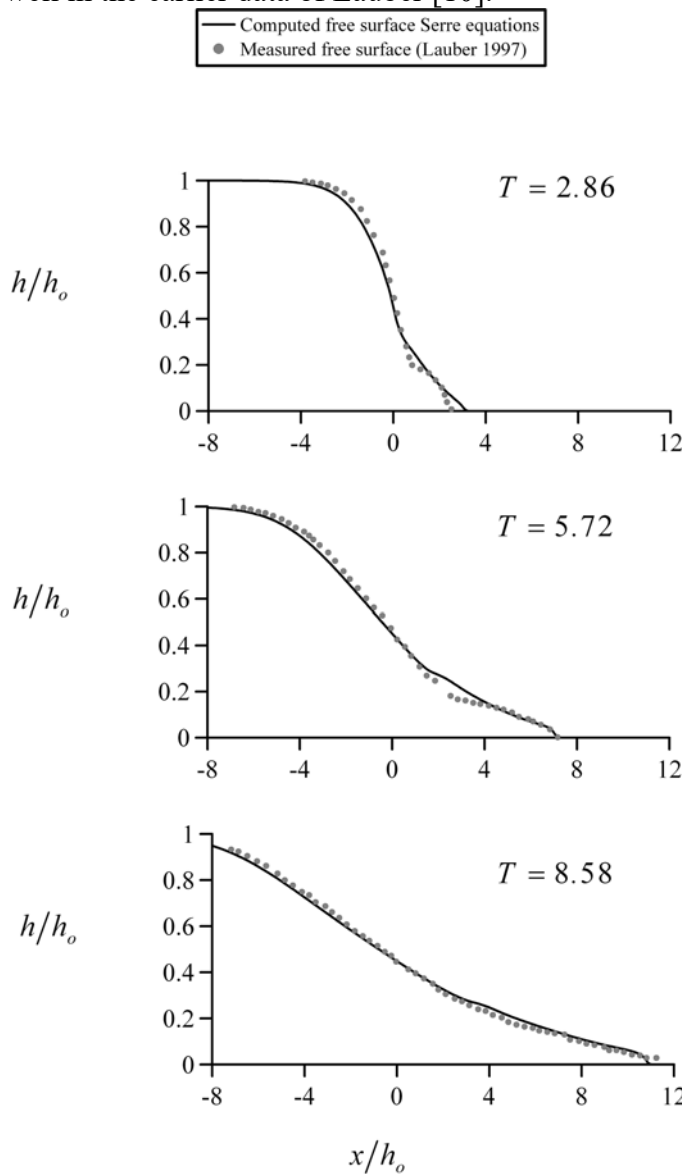


Figure 11. Comparison of computed (Serre equations) and measured [10] wave profiles

The present results should be considered an evidence in favour of adopting the Serre equations in wave propagation problems frequently occurring in civil and environmental engineering. These equations are in fact widely used in coastal engineering and can be extended to other areas of water

research, as suggested here. The present results are not intended to diminish the importance of Ritter's analytical solution: it is a very important tool to check numerical solutions of Saint-Venant equations, and a master development for teaching purposes in courses of hydraulics and fluid mechanics. The original result of Ritter [6], given by Eqs. (3) and (4), is widely known in the literature. The result can be easily check by substitution in Eqs. (1) and (2), and details of the solution process using the method of characteristics can be found in Stoker [50], Jain [3] or Chanson [1]. However, it is less known that in the final part of his paper Ritter [6] acknowledged that his theoretical result was not in agreement with experiments. In fact, he made a sketch of the "real" wave profile similar to those presented with the results of Serre [24] equations in Fig. 9, implying a negative curvature, contrary to the parabolic profile (see Appendix II).

A second set of simulations was considered for comparison purposes with the experimental data of Lauber [10]. While analyzing these experiments it was noted that the gate pull-up motion had a significant effect on the numerical simulations for this dataset. This fact was previously reported by Shigematsu et al. [13], whom conducted numerical simulations using a 2D RANS model, and found that the inclusion of the gate opening movement greatly improved the agreement of numerical computations and their own experimental observations. In his experimental set up, Lauber [10] stated that the upward gate motion was conducted with a vertical acceleration up to 4g. Using this acceleration, and neglecting resistance forces in the gate mechanism, the gate opening time can be easily determined to be  $t_{\text{gate}} = [h_o/(2g)]^{1/2}$ . For Lauber's experiments  $h_o = 0.3$  m, resulting  $t_{\text{gate}} \approx 0.13$ s, or  $T_{\text{gate}} \approx 0.743$ . Clearly, this value cannot be neglected for simulations during the early stages of dam break flows, e.g. for  $T = 2.86$ . Our findings are in agreement with Shigematsu et al. [13], whom determined an empirical gate opening time law for their experiments, which is in fair agreement with the current estimation for  $t_{\text{gate}}$ . Following Shigematsu et al. [13], an approximate method to account for the effect of the gate opening time on numerical simulations was devised here. The gate opening effect was approximately accounted for considering an instantaneous opening in the numerical model, but starting once the gate was fully removed for the channel. Therefore, a time-lag equal to  $t_{\text{gate}}$  was introduced in the numerical simulations. This approximate method was found to produce a significant improvement in the agreement between numerical predictions and observations. The predicted wave profiles using 1300 cells and CFL = 0.1 is compared with observations in Fig. 11, resulting a good agreement.

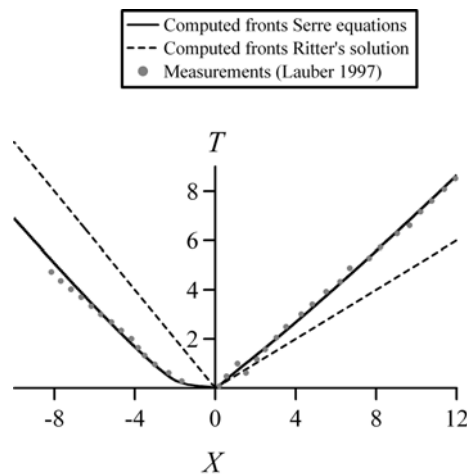


Figure 12. Comparison of computed wave fronts using Serre equations and Ritter [6] analytical solution with measured data [10]

The prediction of the positive and negative wave fronts using the Serre equations is compared in Fig. 12 with measurements by Lauber [10], resulting a good agreement. The gate opening time was again considered as a lag-time for comparative purposes. The edge of the rarefaction wave was defined for practical purposes as the point where  $h = 0.995h_o$ , given that the slope of the computed

wave tends asymptotically to zero near the negative front. Prediction of both fronts using Ritter's theory is also included in the same figure for reference. It can be observed that Ritter's theory overestimated the dry-front position, as previously described [10, 14, 17]. The main physical mechanism from which these discrepancies originate is the friction force at the bed. Computations of the dry-front using Saint-Venant equations produce an almost identical prediction (Fig. 13), confirming that vertical accelerations are not relevant there. The computed edge of the rarefaction wave using Saint-Venant equations is very close to Ritter's. It clearly indicates that friction effects are really negligible there, but vertical accelerations are very important, as confirmed by the good match found using Serre equations in Fig. 12.

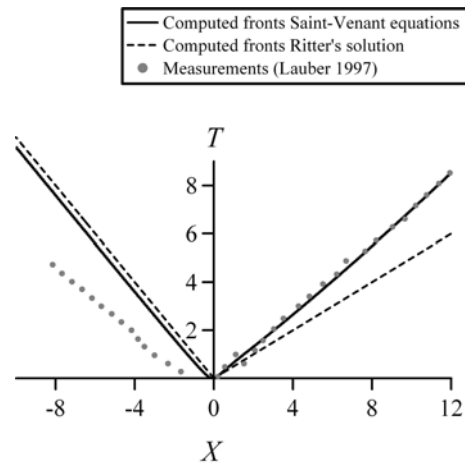


Figure 13. Comparison of computed wave fronts using Saint-Venant equations and Ritter [6] analytical solution with measured data [10]

Finally, the prediction of the dry front using the analytical boundary-layer model [12, 14] is compared in Fig. 14 with experiments [10], resulting a good agreement.

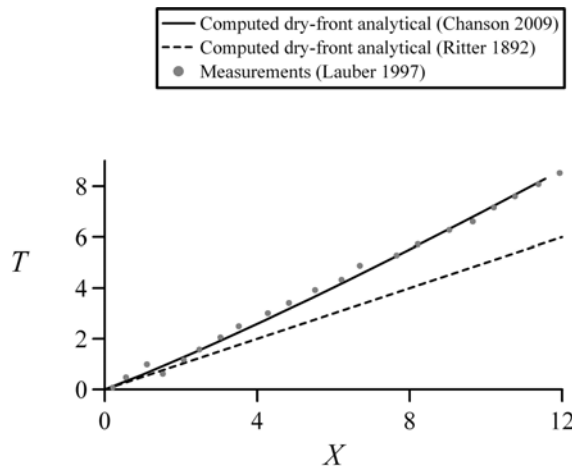


Figure 14. Comparison of computed dry fronts using the boundary-layer model [12, 14] and Ritter [6] analytical solution with measured data [10]

Comparison of simulations using Saint-Venant equations and the Serre-Green-Nagdhi equations indicated that, for engineering purposes, vertical acceleration effects can be neglected for  $T > 40$ . A prominent example where this occurs was already presented in Fig. 4, where the experiments by Schoklitsch [21] are analyzed for  $t = 3.75$  s ( $T = 43.17$ ) and  $t = 9.4$  s ( $T = 108.23$ ). Therefore, long-time simulations of dam break waves can be conducted based on the Saint-Venant equations, but for the initial stage of dam break. During the very initial instants of the dam break waves, vertical

accelerations might be as important as turbulence and bed friction, and cannot be ignored. It is of interest to remark that, in an earlier development by Pohle [51], a two-dimensional solution for Ritter's dam break problem, incorporating thus vertical accelerations, was obtained by formulating the Euler equations in a Lagrangian framework. Using series expansions of time for the particle displacements, and resorting to methods of conformal mapping, a parametric solution for the dam break curves was obtained. This solution is however limited to very small times, e.g.  $T < 0.7$ , and implies a pure vertical motion of the free surface points on the negative wave. Dressler [17] found that Pohle's solution was not in very good agreement with his experimental observations. In contrast, the approximate depth-averaged model used here based on the Serre-Green-Naghdi equations can be applied for  $T > 0.7$ ; it was found to be in good agreement with observations, and it implies only a moderate increase in numerical complexities, as compared to Saint-Venant based models.

#### 4 Conclusions

In this work Ritter's dam-break flow over a dry-bed was revisited, and the following conclusions were obtained:

Two accurate solutions of the viscous dam break wave propagating over a dry-bed were produced using the MUSCL-Hancock finite-volume method and the discontinuous Galerkin finite-element method. Both techniques produced results in excellent agreement. Using this reference numerical solution for the dynamic wave, the Whitham/Dressler/Chanson boundary-layer type conceptual model [11, 12, 14], based on a matching of Ritter's inviscid dynamic wave with a viscous diffusive wave, was established to be a good approximation. It confirms that it is a relevant generalization of Ritter's ideal wave structure. The prediction of the dry-bed front based on the Saint-Venant equations, which rely on the hydrostatic pressure distribution, was found to be good.

The negative wave propagation was however not correctly predicted by the Saint-Venant equations during the initial stages of dam-break waves. Simulations conducted using the Serre-Green-Naghdi equations for fully non-linear and weakly dispersive water waves produces a wave structure in very good agreement with observations; the celerity of the negative wave was much faster than that indicated by Ritter's solution, during the initial instants. The position of the negative wave leading edge was accurately predicted, and the shape of the negative wave, which is not parabolic, was accurately reproduced. In contrast, neither Ritter's analytical solution, nor the numerical solution of Saint-Venant equations, were able to mimic the negative wave features, during the initial instants following a dam break.

It is suggested based on the current results that the numerical solution of Saint-Venant equations, and the Whitham/Dressler/Chanson analytical model as a simplification, can produce a reasonable prediction of dam break waves if the positive wave is the main concern, or for long-time simulations. If both wave fronts need to be tracked then the Serre-Green-Naghdi equations produce results as good of that of Saint-Venant equations for the positive wave, plus an accurate negative wave not reproduced by the latter system. The positive wave front advancing over the initially dry land is governed by friction, whereas the propagation of the water drop upwards in the dam reservoir is controlled by a non-hydrostatic wave motion.

#### Appendix I: Damping model for dispersive terms in Serre-Green-Naghdi equations

Current parametrizations of wave breaking are based on the assumption that the energy dissipation is adequately accounted for by the Rankine-Hugoniot jump conditions of shocks [52, 53, 54]. Therefore, a Boussinesq+Saint Venant matching approach is adopted. Basically, the wave profile is

computed solving the Boussinesq-type equations and, after each time step, a wave breaking criteria is checked in the computational domain. In those cells marked as breaking, the dispersive terms are switched off (equivalent to setting  $\varepsilon = 0$ ), and the SWE are solved there. Other wave-breaking models can be adopted, like the classical diffusive model extensively validated by Cienfuegos et al. [55] or the recent development by Tissier et al. [56]. The wave breaking model proposed by Hosoda and Tada [39] and Hosoda et al. [40], is, however, less known, despite its simplicity and good performance. The idea behind this parametrization is identical to that developed by Tonelli and Petti [41] in the sense that Boussinesq equations are “substituted” by the SWE at breaking cells. However, rather than producing a full (sharp) transition from Boussinesq to the SWE at breaking nodes, they proposed a gradual damping of the dispersive terms when the threshold criteria of wave breaking is exceeded. The method is as simple to implement as that of Tonelli and Petti [41], and permits a very stable behavior of the numerical computations. Below, the physical background of the method is explained.

The idea is to attenuate the dispersive terms of the Serre-Green-Naghdi equations if the local free surface slope exceeds a threshold value. To produce a gradual damping of dispersive terms Hosoda and Tada [39] and Hosoda et al. [40] proposed an exponential attenuation given by

$$\varepsilon = \begin{cases} \exp\left[-\zeta\left(\left|\frac{\partial h}{\partial x}\right| - \left|\frac{\partial h}{\partial x}\right|_{cr}\right)\right] & \text{if } \left|\frac{\partial h}{\partial x}\right| > \left|\frac{\partial h}{\partial x}\right|_{cr}, \\ 1 & \text{else} \end{cases} \quad (48)$$

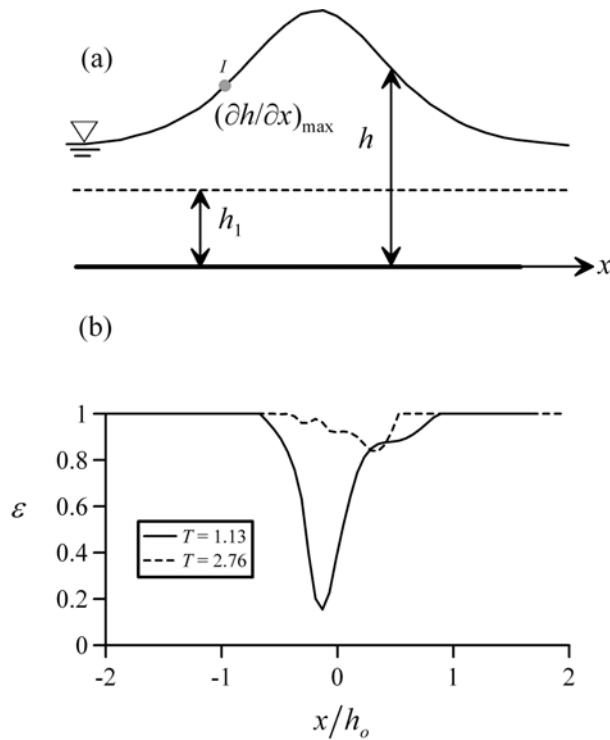


Figure 15. (a) Solitary wave profile (b) evolution of damping factor in test of Fig. 9

A calibration parameter  $\zeta$  is introduced, and  $(\partial h/\partial x)_{cr}$  is the threshold value of the free surface slope above which wave breaking is initiated. This value was determined using the solitary wave as conceptual model, given that it is a particular solution of the Serre-Green-Naghdi equations. The solitary wave profile (Fig. 15a) is given by [24]

$$\frac{h}{h_1} = 1 + (F_1^2 - 1) \operatorname{sech}^2 \left[ \frac{(3F_1^2 - 3)^{1/2}}{F_1} \frac{x}{2h_1} \right], \quad (49)$$

where  $h_1$  is the undisturbed water depth and  $F_1$  the corresponding Froude number. The question is then: What is the maximum value of the free surface slope in a solitary wave for incipient wave breaking? Successive differentiation of Eq. (49) produces

$$\frac{\partial h}{\partial x} = B \operatorname{sech}^2(Ax) \tanh(Ax), \quad \frac{\partial^2 h}{\partial x^2} = AB \operatorname{sech}^2(Ax) [\operatorname{sech}^2(Ax) - 2 \tanh^2(Ax)], \quad (50)$$

where

$$A = \frac{(3F_1^2 - 3)^{1/2}}{2h_1F_1}, \quad B = -(F_1^2 - 1) \frac{(3F_1^2 - 3)^{1/2}}{F_1}. \quad (51)$$

The maximum free surface slope occurs at the inflection point  $I$  in Fig. 15a. Thus, setting  $\partial^2 h / \partial x^2 = 0$  results in

$$x_I = \frac{\ln(2 \pm 3^{1/2})}{2A}, \quad (52)$$

and, using this value of the  $x$ -coordinate, the free surface slope at the inflection point is

$$\left( \frac{\partial h}{\partial x} \right)_{\max} = B \frac{12[(5/3) - 3^{1/2}]}{(3 - 3^{1/2})^3}. \quad (53)$$

Based on undular bore experimental data of Favre waves, the limiting supercritical Froude number for wave breaking  $F_1 = 1.25$  was adopted [39, 40]. Thus, from Eq. (53) results

$$\left| \frac{\partial h}{\partial x} \right|_{cr} = 0.225. \quad (54)$$

This slope is adopted as a threshold value above which wave breaking occurs due to the action of turbulence.

To illustrate the performance of Eq. (48), the test case presented in Fig. 9 is reconsidered in Fig. 15, where  $\varepsilon = \varepsilon(x/h_o)$  is plotted at  $T = 1.13$  and  $2.76$ . Note the low value of  $\varepsilon$  just after the dam break, given that the damping model is activated by the upstream vertical water depth just as soon as computations are initiated. Its action is gradually reduced in magnitude and spatial extension as the wave evolves, given the reduction of the free surface slopes. For the remaining computational snapshots presented in Fig. 9 (e.g.  $T = 3.88, 5.01$  and  $6.64$ ) the damping model is never activated ( $\varepsilon = 1$ ).

## Appendix II: Ritter's original work

In this appendix we reprint two original figures from Ritter [6], given their interest for educational purposes. In Fig. 16 we observe the original parabolic profile sketched by Ritter. The quantity  $(ga)^{1/2}$  is denoted by  $U_o$ , and the celerity of the dry and backward fronts are clearly indicated. The initial water depth in the dam is  $a$ , and the critical water depth at the dam axis is  $(4/9)a$ .

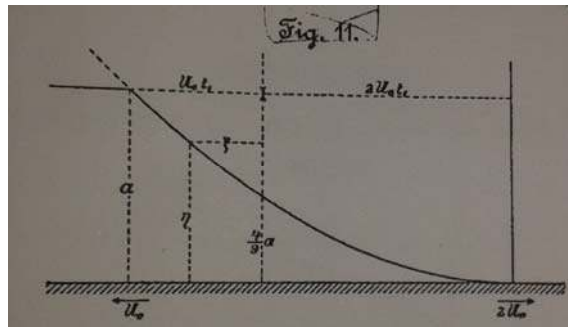


Figure 16 parabolic wave solution by Ritter [6]



Ritter [6] noted that his parabolic profile was not in agreement with observations, and sketched a more realistic shape for the dam break curve, where all the profile has negative curvatures, as seen in Fig. 17.

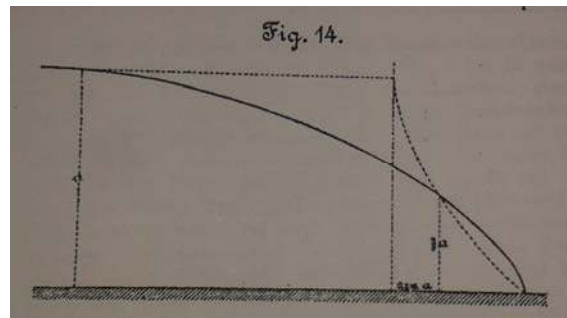


Figure 17 parabolic wave solution and comparison with a more realistic shape for the dam break curve, after Ritter [6]

## References

1. Chanson, H. (2004). *The hydraulics of open channel flows: An introduction*. Butterworth-Heinemann, Oxford, UK.
2. Ré, R. (1946). Étude du lâcher instantané d'une retenue d'eau dans un canal par la méthode graphique. *La Houille Blanche*, 1(3), 181-188.
3. Jain, S.C. (2001). *Open channel flow*. John Wiley & Sons, New York.
4. Sun, S., Leng, X., Chanson, H. (2016). Rapid operation of a tainter gate: Generation process and initial upstream surge motion. *Environmental Fluid Mechanics*, 16(1), 87-100 (DOI: 10.1007/s10652-015-9414-3).
5. Toro, E. F. (2001). *Shock-capturing methods for free-surface shallow flows*. John Wiley and Sons, Singapore.
6. Ritter, A. (1892). Die Fortpflanzung von Wasserwellen. *Zeitschrift Verein Deutscher Ingenieure*, 36(2), 947-954.
7. Khan, A. A., Lai, W. (2014). *Modeling shallow water flows using the discontinuous Galerkin method*. CRC Press, Taylor and Francis, New York.
8. Barré de Saint-Venant, A. J. C. (1871). Théorie du mouvement non permanent des eaux, avec application aux crues des rivières et à l'introduction des marées dans leur lit. *Comptes Rendus des séances de l'Académie des Sciences* 73, 147-154.
9. Toro, E. F. (2009). *Riemann solvers and numerical methods for fluid dynamics: A practical introduction*. Springer, Berlin, Germany.
10. Lauber, G. (1997). *Experimente zur Talsperrenbruchwelle im glatten geneigten Rechteckkanal*, VAW-ETH, Ph.D. thesis, Zürich, Switzerland.
11. Dressler, R. F. (1952). Hydraulic resistance effect upon the dambreak functions. *J. Res. Natl. Bureau of Standards*, 49(3), 217-225.
12. Whitham, G. B. (1955). The effects of hydraulic resistance in the dam-break problem. *Proc. Roy. Soc. of London*, 227(Serie A), 399-407.
13. Shigematsu, T., Liu, P.-F., Oda, K. (2004). Numerical modeling of the initial stages of dam-break waves. *J. Hydraulic Res.* 42(2), 183-195.
14. Chanson, H. (2009). Application of the method of characteristics to the dam break problem. *J. Hydraulic Res.* 47(1), 41-49 (DOI: 10.3826/jhr.2009.2865).
15. Lauber, G., Hager, W.H. (1998). Experiments to dambreak wave: horizontal channel. *J. Hydraulic Res.* 36(3), 291-307.
16. Oertel, M., Bung, D.B. (2012). Initial stage of two-dimensional dam-break waves: laboratory versus VOF. *J. Hydraulic Res.* 50(1), 89-97.

17. Dressler, R. (1954). Comparison of theories and experiments for the hydraulic dam-break wave. *Proc. Int. Assoc. Scientific Hydrology Assemblée Générale* Vol. 3 (38), 319-328, Rome, Italy.
18. Steffler, P.M., Jin, Y.C. (1993). Depth-averaged and moment equations for moderately shallow free surface flow. *J. Hydraul. Res.*, 31(1), 5-17.
19. Khan, A. A., Steffler, P. M. (1996). Vertically averaged and moment equations model for flow over curved beds. *J. Hydraul. Engng.*, 122(1), 3-9.
20. LeVeque, R.J. (2002). *Finite volume methods for hyperbolic problems*. Cambridge Univ. Press, New York.
21. Schoklitsch, A. (1917). Über dambruchwellen. *Kaiserliche Akademie der Wissenschaften, Wien, Mathematisch-Naturwissenschaftliche Klasse, Sitzungberichte IIa*, 126, 1489-1514.
22. Hesthaven, J.S., Warburton, T (2008). *Nodal discontinuous Galerkin methods: Algorithms, analysis, and applications*. Texts in Applied Mathematics 44, Springer, New York.
23. Hoffman, J.D. (2001). *Numerical methods for engineers and scientists*. Second edition, Marcel Dekker, New York.
24. Serre, F. (1953). Contribution à l'étude des écoulements permanents et variables dans les canaux. *La Houille Blanche*, 8(6-7), 374-388; 8(12), 830-887.
25. Su, C. H., Gardner, C. S. (1969). KDV equation and generalizations. Part III. Derivation of Korteweg-de Vries equation and Burgers equation. *J. Math. Phys.*, 10(3), 536-539.
26. Green, A.E., Naghdi, P.M. (1976). Directed fluid sheets. *Proc. R. Soc. London A* 347, 447-473.
27. Green, A.E., Naghdi, P.M. (1976). A derivation of equations for wave propagation in water of variable depth. *J. Fluid Mech.* 78, 237-246.
28. Castro-Orgaz, O., and Hager, W. H. (2014). 1D modelling of curvilinear free surface flow: Generalized Matthew theory. *J. Hydraul. Res.*, 52(1), 14-23.
29. Mohapatra, P.K., Chaudhry, M.H. (2004). Numerical solution of Boussinesq equations to simulate dam-break flows. *J. Hydraulic Engng.* 130(2), 156-159.
30. Barthélemy, E. (2004). Nonlinear shallow water theories for coastal waters. *Surveys in Geophysics*, 25(3), 315-337.
31. Cienfuegos, R., Barthélemy, E., Bonneton, P. (2006). A fourth-order compact finite volume scheme for fully nonlinear and weakly dispersive Boussinesq-type equations. Part I: Model development and analysis. *Int. J. Num. Meth. Fluids*, 51(11), 1217-1253.
32. Dias, F., Milewski, P. (2010). On the fully non-linear shallow-water generalized Serre equations. *Physics Letters A* 374(8), 1049-1053.
33. Bonneton, P., Chazel, F., Lannes, D., Marche, F., and Tissier, M. (2011). A splitting approach for the fully nonlinear and weakly dispersive Green-Naghdi model. *J. Computational Phys.*, 230(4), 1479-1498.
34. Castro-Orgaz, O., Chanson, H. (2011). Near-critical free surface flows: Real fluid flow analysis. *Environmental Fluid Mechanics*, 11(5), 499-516 (DOI: 10.1007/s10652-010-9192-x).
35. Nakagawa, H., Nakamura, S., Ichihashi, K. (1969). Generation and development of a hydraulic bore due to the breaking of a dam. *Bull. Disas. Prev. Inst. Kyoto Univ.* 19(154), 1-17.
36. Betamio de Almeida, A., Bento Franco, A. (1994). Modeling of dam-break flow. Chapter in *Computer Modelling of Free Surface and Pressurized Flows*, pp. 343-373, Nato Science Series E, Springer, Berlin, Germany.
37. Stansby, P. K., Chegini, A., and Barnes, T. C. D. (1998). The initial stages of dam-break flow. *J. Fluid Mech.*, 374, 407-424.
38. Mohapatra, P.K., Eswaran, V., Murthy Bhallamudi, S. (1999). Two-dimensional analysis of dam-break flow in a vertical plane. *J. Hydraulic Engng.* 125(2), 183-192.
39. Hosoda, T., Tada, A. (1994). Free surface profile analysis on open channel flow by means of 1-D basic equations with effect of vertical acceleration. *JSCE Annual J. Hydraul. Engng.*, 38, 457-462.

- 803 40. Hosoda, T., Tada, A., Inoue, K., Kitahara, M. (1994). Hydraulic analysis of unsteady flows with  
804 propagation of an interface between free surface flow and pressurized flow. *Doboku Gakkai*  
805 *Ronbunshu* vol. 503/II-29, 89-97.
- 806 41. Tonelli, M., Petti, M. (2009). Hybrid finite volume - finite difference scheme for 2DH improved  
807 Boussinesq equations. *Coastal Eng.*, 56(5-6), 609-620.
- 808 42. Wei, G., Kirby, J.T., Grilli, S.T., Subramanya, R. (1995). A fully nonlinear Boussinesq model  
809 for surface waves 1: Highly nonlinear unsteady waves. *J. Fluid Mech.* 294, 71-92.
- 810 43. Erduran, K. S., Ilic, S., and Kutija, V. (2005). Hybrid finite-volume finite-difference scheme for  
811 the solution of Boussinesq equations. *Int. J. Num. Meth. Fluids*, 49(11), 1213-1232.
- 812 44. Kim, D.-H., Lynett, P.J. (2011). Dispersive and nonhydrostatic pressure effects at the front of  
813 surge. *J. Hydraulic Engng.* 137(7), 754-765.
- 814 45. Hosoda, T., Iwata, M., Muramoto, Y., Furuhashi, T. (1997). Hydraulic analysis of undular bore  
815 in open channels with circular cross-section. *JSCE Annual J. Hydraul. Engng.*, 41, 645-650.
- 816 46. Bashiri Atrabi, H., Hosoda, T., Tada, A. (2015). Simulation of air cavity bubble advancing into  
817 a straight duct. *J. Hydraulic Engng.* 141(1), 04014068-1-04014068-9.
- 818 47. Denlinger, R.P., O'Connell, D.R.H. (2008). Computing nonhydrostatic shallow-water flow over  
819 steep terrain. *J. Hydraulic Engng.* 134(11), 1590-1602.
- 820 48. Ozmen-Cagatay, H., Kocaman, S. (2010). Dam-break flows during initial stage using SWE and  
821 RANS approaches. *J. Hydraul. Res.*, 48(5), 603-611.
- 822 49. Leng, X., Chanson, H. (2015). Unsteady turbulence in expansion waves in rivers and estuaries:  
823 an experimental study. *Environmental Fluid Mechanics*, 15(5), 905-922 (DOI:  
824 10.1007/s10652-014-9385-9)
- 825 50. Stoker, J. J. (1957). *Water waves: The mathematical theories with applications*. John Wiley and  
826 Sons, New York.
- 827 51. Phole, F.V. (1952). Motion of water due to breaking of a dam and related problems. *Symposium*  
828 *on Gravity Waves*, paper n°8, 47-53.
- 829 52. Brocchini, M. (2013). A reasoned overview on Boussinesq-type models: the interplay between  
830 physics, mathematics and numerics. *Proc. Roy. Soc. A*, 469, 20130496.
- 831 53. Kirby, J.T. (2016). Boussinesq models and their application to coastal processes across a wide  
832 range of scales. *J. Water, Port, Coastal and Coastal Engng.*, 142(6): 03116005.
- 833 54. Lubin, P., Chanson, H. (2016). Are breaking waves, bores, surges and jumps the same flow?.  
834 *Env. Fluid Mech.* doi:10.1007/s10652-016-9475-y.
- 835 55. Cienfuegos, R, Barthélemy, E, Bonneton, P (2010). Wave-breaking model for boussinesq-type  
836 equations including roller effects in the mass conservation equation. *J Waterw Port Coast*  
837 *Ocean Engng.* 136(1):10-26.
- 838 56. Tissier, M, Bonneton, P, Marche, F, Lannes, D (2012). A new approach to handle wave  
839 breaking in fully non-linear Boussinesq models. *Coast Eng* 67:54-66.
- 840